Daniel A. Porter* and Thomas A. Berfield

Constraint Effects on Torque-Actuated Bistable Energy Harvesters

DOI 10.1515/ehs-2015-0009

Abstract: The effect of boundary conditions on a bistable device that buckles into an "S" shape and utilizes polyvinylidene fluoride is evaluated. Four permutations with different center constraints are the perfectly pinned circular steel, rigid glued circular steel, 3×1 and 5×1 3D printed rectangle polylactic acid prototypes. Using a load of 30 MΩ, which was close to the optimal load resistance, frequency sweeps in the forward and reverse directions indicated different nonlinearities depending on if the device is buckled or not. Peak resonant frequencies for the devices are around 18 to 30 Hz with bistable actuation occurring as low as 0.3 g_{rms}. Damping was measured using logarithmic decrement, linear and nonlinear half-power methods. Results showed that the devices have an average damping ratio of 4.1%. The buckled 3×1 mm device with short compliance arms generated 12.6 μW at 21.1 Hz when swept forward at 0.4 g_{rms} and had the highest figure-of-merit (FoM_{BW}) metric of all devices tested. Unbuckled devices tended to exhibit a spring stiffening nonlinearity while buckled devices obtained higher power outputs in the forward direction but could have their operating frequencies significantly lowered if swept backward. All buckled devices tested during a chirp input could be promoted to high-energy orbits for enhanced performance.

Keywords: bistable, buckled, energy harvesting, polyvinylidene fluoride, PVDF, snap-through, VEH

Introduction

By converting environment mechanical vibrations or forces into electrical power, energy harvesters can drive active sensors without the need to be tethered to a constant power source or periodically serviced to change batteries. This is a critical trait for numerous applications, such as wireless sensor networks (WSN) or biomedical implants that disallow the use of wires or are located in difficult to access locations. One such example of a dangerous and expensive area to replace batteries is in pacemakers where surgery is needed to service the device power supply.

Structural health monitoring is another prime target application area for energy harvesters where low-power transmission for sensor data via Bluetooth is feasible (Amin Karami and Inman 2012; Dementyev et al. 2013). Increasing the performance and capabilities of energy harvesting devices is an increasing topic of interest and could also benefit the global community through reduced battery waste and large-scale energy harvesting (Zuo and Tang 2013).

Nonlinear energy harvesters offer an advantage over their linear-response counterparts by means of wider bandwidths (Harne and Wang 2013; Twiefel and Westermann 2013), higher voltage and power outputs (Xu et al. 2013; Jiang et al. 2010) and the ability to operate in high-energy periodic orbits (Erturk and Inman 2011). One of the most recent advances in nonlinear energy harvesters include a tristable device (Trigona et al. 2013) that shows promise in the presence of white Gaussian noise.

Buckled structures have also been investigated as a means of inducing nonlinear responses. Zheng et al. created an offset doubly clamped polyvinylidene fluoride (PVDF) strip at the base of a cantilever beam to amplify strain and compared it with a sandwiched strip directly adhered to the bottom. When optimized and undergoing large axial stresses, the device outperformed the nonbuckled sandwiched beam (Zheng et al. 2014). Cottone et al. used a doubly clamped bistable beam which utilized a magnet housing as the center mass. It was found that the buckled beam performed slightly better away from the resonant region than the unbuckled beam (Cottone et al. 2014). Another bistable buckled beam device was constructed by Ando et al. and used impact piezoelectric transducers to capture energy from snap-through behavior (Ando et al. 2014). A bistable buckled energy harvesting device introduced by the authors (Porter and Berfield 2014) has also demonstrated promising power scavenging characteristics at low frequencies (< 30 Hz) by utilizing a torque arm mechanism to induce buckled state switching. The investigated

***Corresponding author: Daniel A. Porter,** Department of Mechanical Engineering, University of Louisville, Louisville, KY 40292, USA,
E-mail: daport02@louisville.edu
http://orcid.org/0000-0002-4219-3782
Thomas A. Berfield, Department of Mechanical Engineering, University of Louisville, Louisville, KY 40292, USA,
E-mail: tom.berfield@louisville.edu

structure and the associated nonlinear response are scalable to the microelectromechanical systems (MEMS) regime. Since inertial effects scale with length cubed (L^3), the torque arm amplification effect is essential for maintaining the same operational functionality demonstrated at the macroscale. In addition, the basic design is fairly planar which provides compatibility with standard microfabrication methods. Magnetic bistable energy harvesters are not as easily scaled to the MEMS regime due to fabrication process compatibility issues associated with required material deposition temperatures, post treatments and oxidations, in addition to basic limitations on coil size and design complexity (Wang 2010; Allen 2005; Percy et al. 2014). This work focuses on performance optimization of the torque arm-actuated energy harvesting device, examining effects of geometry and constraint conditions, as well as determining optimal loads and nonlinear damping ratios. In addition, the dynamic conditions for promoting entrance into high-energy orbits (HEOs) are investigated.

Methods

Design Considerations and Specifications of Fabricated Devices

The energy harvester of interest operates on the basic premise that proof masses mounted on cantilevered arms transfer torque to the mid-section of a central compressively buckled beam with piezoelectric PVDF strips adhered. A schematic of the device is shown in Figure 1. Upon compression of the center beam, quasi-pinned compliance arm supports induce "S"-shaped buckled deflection profiles of the center beam. Transverse motion (vibration) of the structure base introduces a moment at the center of the "S" shape and can induce switching between buckled states for sufficiently large accelerations. Snap-through (switching between buckled stable states) is desirable for potentially generating large strains within the central piezoelectric strips and maximizing power output.

Ideally, compliance arms that act as a perfect pin constraint would provide optimal torque transfer to the center and allow snap-through to be exhibited at the lowest possible acceleration levels. However, mimicking a perfectly pinned condition at the center beam adds fabrication cost/difficulty and is not feasible for planned MEMS-scale versions of the device. Using anything but a perfectly pinned method to constrain the deflection of the center beam will add both torsional and potential out-of-plane compliance. Torsional stiffness of the compliance arm will reduce the amount of force transferred to the center beam, increasing the energy threshold to be overcome to create stability state switching. Vertical compliance can change the buckling force needed to make the device bistable, increasing the acceleration needed to induce snap-through or pushing the center beam into first buckled mode deflection profile (dome shape) rather than the "S"-shaped second mode shown in Figure 1(c).

To test the effects of the compliance arm constraint and geometrical parameters, four device variations were constructed. The first device was a pinned beam that used a greased 20 gauge steel rod running through the entire center body width that allowed nearly free rotation at the compliance arm supports (Figure 1(f)). The second device was nearly identical to the first with the exception of the compliance arm constraint. In this case, the compliance arm rod was locked to the central beam using an industrial adhesive (JB-Weld Compound 8265-S), in addition to clamping at the base supports. The result was a clamped–clamped compliance arm made of steel with a round cross section. The third and fourth devices used 3×1 mm and 5×1 mm cross-sectional polylactic acid (PLA) compliance arms, respectively, with 2 mm fillets near the brace structure (Figure 1(g)–(h)). In all cases, 5/16″ steel nuts (4.62 g) were used as proof masses and were adhered 10 mm from the tip of the brace as shown in Figure 1.

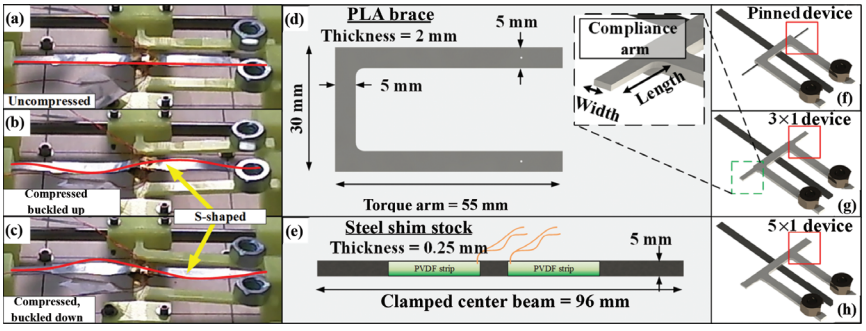

Figure 1: 3×1 device in the (a) uncompressed, (b) compressed buckled up and (c) compressed buckled down. Main components of energy harvesting device, including the (d) torque arm PLA brace, the (e) steel shim stock center beam with PVDF strips, and the compliance arms constructed in the (f) pinned, (d) 3×1, and (g) 5×1 configurations.

Piezoelectric strips of 0.11 mm thickness (GoodFellow FV301960/3, $d_{31} = 19$ pC N^{-1}, $d_{33} = -20$ pC N^{-1}) were cut to a width and length of 5 and 33 mm, respectively. Previous finite element analysis (FEA) results on the buckled center beam (Porter and Berfield, 2014) show that a strain sign change occurs at about 16% of the beam length from the end constraints and at the middle for these devices. Thus, to minimize charge neutralization, two separate strips of PVDF are adhered to the center beam on spans of one-sixth to one-half along the length of the beam, and again on a span from one-half to five-sixths of the beam (Figure 1(b)).

Shaker Table Setup

A custom-built shaker table setup was construed to test the devices under sinusoidal driving conditions. The shaker consisted of a 250 W_{p-p} (peak-to-peak) speaker, a 200 W_{rms} (root mean squared) amplifier, Arduino Nana v3.0 microcontroller, MPU-6050 accelerometer, and an op-amp signal buffer and conditioning circuit. The buffer and conditioning circuit are needed to accept a moderately high-voltage response and provide a high-input impedance so that the power generated can be accurately measured. To accommodate the large impedance loads that accompany single layer element PVDF strips (Jiang et al. 2010; Wen et al. 2014), a two-stage op-amp buffer circuit was used with an input impedance over 1 GΩ (OPA551PA). Driving specifications used in this work for the system were 10–500 Hz and 0.1–3 g_{rms} while the logging specifications for the Arduino utilized four voltage channels running 2,048 S/s.

A compression rig mounted atop the shaker plate allowed for each device to have variable length compliance arms and the ability to fine-tune a compression displacement by turning 8–32″ push rods and then locking down the rig by tightening M3 bolts. Compression displacement measurements for the system were performed via calipers. A render of the designed shaker table and the as-fabricated system with the 3×1 mm device and 8 mm compliance arms in the uncompressed state are shown in Figure 2. Great care was taken to buckle the device symmetrically as the shape of the potential energy function (specifically the maximum deflection point of the center beam which must be traversed to exhibit snap-through) must be within a certain range to provide energy harvesting benefits (Masana and Daqaq 2011). Near the critical buckling load, the resonant frequency of the center beam should theoretically approach zero and afterward stiffen up as more compression is applied (Masana and Daqaq 2013).

Optimum Load

To evaluate devices at peak power performance conditions, the optimum load was determined. PVDF strips with single electrodes tend to have high optimum resistance driving loads. This can introduce difficulties as the input impedance on standard laboratory testing equipment can be on the same scale as the devices being tested, which in turn can create power sharing that diminishes the signal. To reduce the optimum load of PVDF, multiple stacked PVDF and electrode layers can be used but the amount of layers needed would be very costly.

Four test cases were run at different impedance loads to determine the optimum load conditions for which all other tests would be performed. Three of the cases included the uncompressed pinned, 3×1 mm and 5×1 mm devices while the last test case was a compressed 3×1 mm device. All optimum load cases were run at 0.5 g_{rms} and near resonance.

A plot of normalized voltage response versus load impedance is shown in Figure 3. Optimum values ranged from around 20 to 40 MΩ. Since all tests showed minimal drop-off in power performance around 30 MΩ, 30 MΩ was chosen as the driving resistance load for all devices and testing cases.

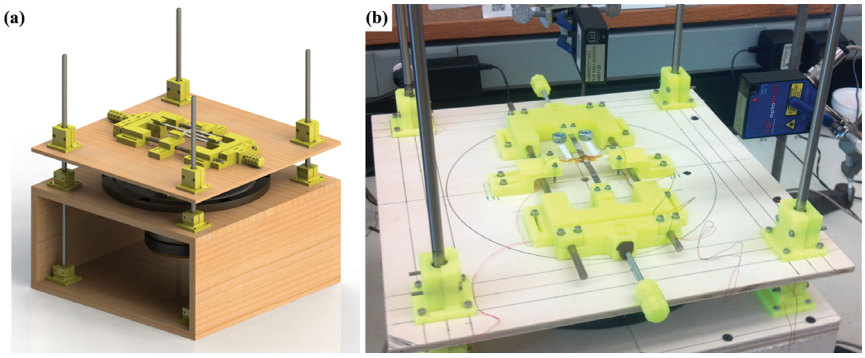

Figure 2: (a) Render of designed shaker table and (b) the as-fabricated shaker table with 3×1 device mounted.

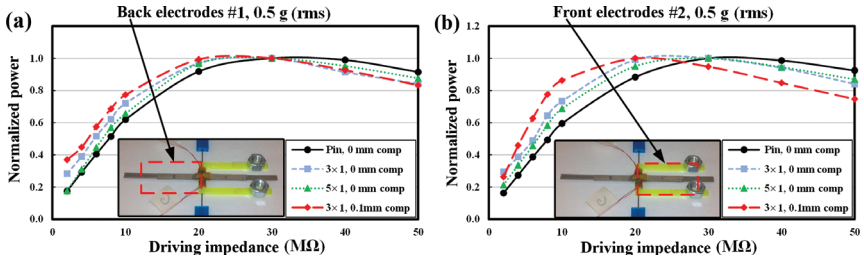

Figure 3: Normalized voltage response versus load impedance for the (a) back and (b) front electrode, all tested using 8 mm compliance arms.

Evaluation of Damping

Damping is a desirable parameter to quantify so that accurate simulations can be constructed and verified, in turn enabling optimization of device performance. Due to the large displacements that this device undergoes and the allowed range of motion for the displacement sensors, damping for low input accelerations is evaluated. Damping during very large motions would require a 3D digital image correlation (DIC) system. Viscous damping was evaluated for the device using three different methods: free, linear forced and nonlinear forced. Free vibration analysis works well for decaying responses, but can be a poor representation of damping in energy harvesting structures that have a constant input function exerted upon them. Despite this limitation, values for free damping were extracted using the voltage response to a monopulse chirp sent to the shaker table and using the logarithmic decrement method in eq. [1] Beards (1995):

$$\zeta_{\text{free}} = \frac{1}{\sqrt{1+\left(\frac{2\pi}{\ln(x_0/x_1)}\right)^2}} \quad [1]$$

where x_0 and x_1 are the amplitudes of the decaying sine wave at the beginning and end of each successive cycles, respectively.

A more realistic evaluation of linear viscous damping is to use the half-power bandwidth (HPB) method which evaluates the quality and damping ratio for a linear system (Beards 1995). This process requires the displacement measurement of the base shaker table and the tip of the torque arms, which was performed using two micro-epsilon laser displacement sensors (Micro-Epsilon NCDT1401). The gain, which is the ratio of the tip displacement to the base displacement, can be plotted against frequency to form a bode plot. From this plot, the linear quality factor can be determined using (Beards 1995)

$$Q_{\text{forced,l}} = \frac{f_{\text{r}}}{f_2 - f_1} \quad [2]$$

where f_{r} is the resonant frequency, f_1 is the first −3 dB drop down point and f_2 is the second. The damping ratio can then be determined from $\zeta = 1/2Q$. The buckled energy harvester device tested here was found to be nonlinear in both the uncompressed and compressed states, exhibiting a spring-stiffening or spring-softening effect characterized by a jump discontinuity. Physically, this means the frequency response depends on the direction of frequency sweeping. An even better estimate of the damping for a nonlinear system is to use a modified version of the HPB from Davis (2011)

$$Q_{\text{forced,nl}} = \frac{f_{\text{p}}}{f_{\text{jd2}} - f_{\text{jd1}}}\sqrt{n^2 - 1} \quad [3]$$

where f_{p} is the peak gain frequency, f_{jd1} is the frequency of the jump down point, f_{jd2} is the frequency of the jump down point that has the same gain as f_{jd1}. The value n is the ratio of the gain of f_{p} and f_{jd1}. It is important to know which type of nonlinearity, stiffening or softening, the system falls under because one peak will be larger than the other during the directional sweep.

Parametric Evaluation of Compliance Arms

A parametric evaluation of the effect of compliance arm geometry on device behavior was performed using the length and the width of the arms as parameters. For clarity, a naming scheme was selected based on the arm width, with devices named as 3×1 and 5×1 referring to 3 mm × 1 mm cross section and 5 mm × 1 mm cross section, etc. The other two device variations were named for their free pinned or completely glued 20 gauge steel support. For the pinned, glued, 3×1, 5×1 the compliance length was varied between 8 and 12.5 mm. The 3×1 device was also tested in a 3 mm length setup as an additional run. Each device was frequency swept both forward and backward from 0.2 to 0.6 g_{rms} with a frequency range of 10–35 Hz.

ANSYS Modal Frequency Simulations

To get a rough estimate of the resonant frequencies for the fabricated devices, an ANSYS modal analysis was

used. ANSYS linearizes all contact and nonlinear effects when estimating a modal frequency or harmonic sweep response. To capture more accurate, nonlinear responses for the devices, a transient analysis would be needed with a linearly varying frequency acceleration load. If the device exhibits snap-through under the simulated driving conditions, then the model would require a very small time step increment to capture this large displacement event. Due to the large computational times required to perform resonant frequency estimates under such snap-through conditions, these cases were not considered.

The model consisted of 8-node SHELL281 elements for the center beam and 20-node SOLID95 elements for the PLA brace and proof masses. Two cases were run for each device in which one had no compression and the other had a total of 0.1 mm of compression for the prestressed state. One item of great interest was the proximity of the second mode (each torque arm being 180° out of phase) to the first mode in terms of frequency, as the second mode tends to be detrimental to the power output of the device.

Promotion into HEOs

Nonlinear buckled devices such as the prototypes evaluated in this article generally exhibit chaotic behavior in response to an acceleration input. Normal, low-energy, snap-through behavior is governed by strange attractors that demonstrate stochastic voltage responses and provide little benefit in terms of peak rms power generation. However, if extra energy is put into the system, the device investigated herein can be pushed into a more periodic, HEO state that can be maintained. Associated with these HEOs are very large displacement amplitudes that may increase power performance and/or bandwidth for a given input acceleration when compared to the same device in the unbuckled state.

The buckled devices probed in this work were promoted into HEOs by generating a Gaussian input monopulse three times as high as the driving sinusoidal audio wave and superimposing it onto this signal in phase. The result created a rapidly decaying acceleration chirp or impulse that momentarily pushed the device at a higher acceleration. Based on previous works (Erturk and Inman 2011), it was theorized that this impulse would provide sufficient additional energy into the structure to enter an HEO state and increase device performance when compared with the same device in the unbuckled state.

Results

Damping Effects

Free vibration tests were performed for the majority of the vibrational energy harvester (VEH) devices. After a monopulse was applied to the stationary device, the output voltage recorded typically appeared to be similar to a decaying sine wave. In the logarithmic decrement method, only peaks in the signal obtained after the base accelerometer had come to rest are used to determine damping behavior. Conversely, the nonlinear half-power method analysis is slightly more complicated due to deviations in devices performance based on sweep direction. Graphs for the logarithmic decrement and half-power method are shown in Figure 4 for the 3×1 mm device with 8 mm compliance arms. Sweeps for a few of the devices in their various configurations are shown in Table 1. An additional compressed case for the 5×1 mm device was also performed to investigate effects of damping on an over-compressed prototype. As seen below, over-compression tends to increase damping which is highly detrimental to device power performance. If the over-compressed case is neglected, the average dampening for all of the nonlinear devices combined is approximately 4.1%. This is a good starting estimate for FEA analysis. The results indicate that slight buckling on compliant structures should not change the damping ratio by much.

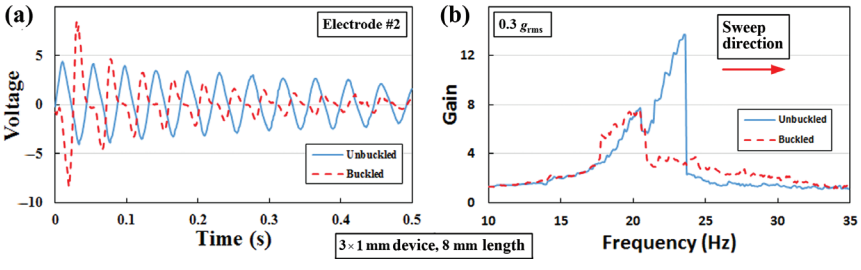

Figure 4: (a) Voltage output and (b) gain response plots for the 3×1 mm device with 8 mm compliance arms.

Table 1: Damping ratios for the tested compressed and uncompressed devices using different methods.

	Compliance length = 8 mm	Forward, compliance length = 8 mm		Reverse, compliance length = 8 mm		Forward, compliance length = 12.5 mm		Reverse, compliance length = 12.5 mm	
	Free	Forced linear	Forced nonlinear	Forced linear	Forced nonlinear	Forced linear	Forced nonlinear	Forced linear	Forced nonlinear
Glue, 0 mm comp.		0.056	0.042	0.037	0.035	0.029	0.026	0.016	0.025
Glue, 0.1 mm comp.		0.059	0.041	0.078	0.050	0.095	0.080	0.075	0.054
Pin, 0 mm comp.	0.023	0.037	0.045			0.034	0.041		
Pin, 0.1 mm comp.	0.040	0.051	0.053			0.045	0.039		
3 × 1 0 mm comp.	0.009	0.034	0.035	0.066	0.050	0.022	0.026	0.060	0.059
3 × 1 0.1 mm comp.	0.061	0.071	0.048			0.047	0.028		
5 × 1 0 mm comp.	0.015	0.039	0.032			0.033	0.038		
5 × 1 0.1 mm comp.	0.046	0.032	0.029			0.032	0.046		
5 × 1 0.2 mm comp.		0.095	0.066			0.067	0.056		

Power Generation

Forward and reverse sweeps of all devices were performed while recording V_{pp} and V_{rms} voltages. Another interesting parameter is the full width at half max (FWHM) value of the sweep and is calculated by measuring the width of the peak (in Hz) at half of the maximum resonant value. This parameter provides an indication of device operating bandwidth. Data from the sweeps of the 3 × 1 mm device with the 8 mm compliance arm length configuration are shown in Figure 5. It should be noted that the V_{rms} amplitude increases greatly once snap-through behavior initiates for the buckled cases and that the response of the unbuckled devices looks inherently nonlinear. Such behavior can be caused by large out-of-plane displacements or imperfect boundary conditions (Spreemann, Folkmer, and Manoli 2011).

Power output is one of the critical, useful metrics for evaluating energy harvesting device performance. The rms power (P_{rms}) from the PVDF strip voltage is

$$P_{rms} = \frac{{V_{rms}}^2}{R} \quad [4]$$

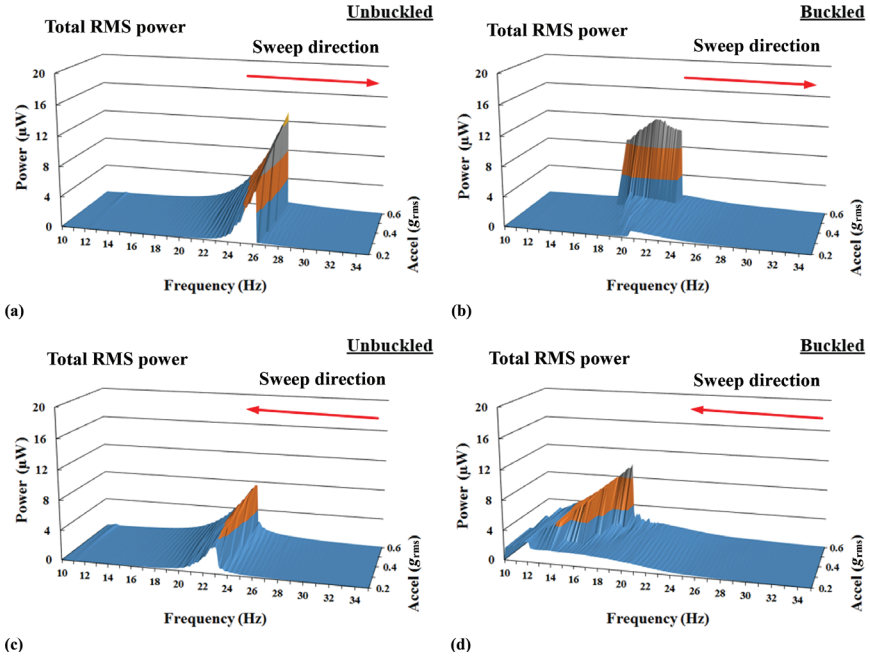

Figure 5: Power results for the 3 × 1 mm device in the (a) unbuckled forward sweep, (b) buckled forward sweep, (c) unbuckled reverse sweep and (d) buckled reverse sweep case. Compliance arms are 8 mm long.

where R is the load resistance used for each piezoelectric strip (30 MΩ). General results for the peak resonant frequency, the linear modal frequencies and P_{rms} are shown in Tables 2 and 3. Italic and superscript (a) elements show the acceleration and sweep cycles, where snap-through behavior was identified.

Snap-through action almost always tended to increase P_{rms} values for the devices when compared with their

Table 2: Forward sweep data for all devices tested.

Forward sweep →	Total width (mm)	Compliance length (mm)	Compression (mm)	Fr peak avg (Hz)	FEA Fn (Hz), $\zeta = 0$	% Diff.	RMS power (μW)				
							0.2	0.3	0.4	0.5	0.6
Glued pin device	46	8	0	28.58	31.29	−8.70	0.77	1.15	1.53	2.07	2.57
Glued pin device	55	12.5	0	28.08	29.68	−5.40	1.41	2.20	2.93	3.62	4.26
Glued pin device	46	8	0.1	27.62	31.17	−11.4	0.94	1.44	2.03	2.22	2.66
Glued pin device	55	12.5	0.1	23.02	29.93	−23.1	1.48	3.40	5.05[a]	5.92[a]	6.63[a]
Pure pin device	46	8	0	23.76	22.82	4.10	4.22	5.61	7.19	6.31	5.54
Pure pin device	55	12.5	0	23.06	22.41	2.90	3.79	5.00	6.41	5.62	6.10
Pure pin device	46	8	0.1	18.26	23.41	−22.0	1.25	1.40	1.50	10.40[a]	11.20[a]
Pure pin device	55	12.5	0.1	17.98	23.20	−22.5	1.09	1.37	1.69	9.46[a]	10.10[a]
3 × 1 mm compliance	36	3	0	24.70	25.43	−2.90	5.87	7.75	9.54	10.50	12.00
3 × 1 mm compliance	46	8	0	26.5	20.89	26.90	6.77	8.81	10.90	11.70	13.30
3 × 1 mm compliance	55	12.5	0	24.54	19.85	23.70	6.69	8.36	10.20	11.30	12.80
3 × 1 mm compliance	36	3	0.1	18.70	25.27	−26.00	0.82	1.23	12.60[a]	12.30[a]	12.00[a]
3 × 1 mm compliance	46	8	0.1	19.74	22.57	−12.50	0.95	1.36	1.58	2.39	11.70[a]
3 × 1 mm compliance	55	12.5	0.1	20.46	21.80	−6.10	0.97	1.37	1.73	2.02	3.03
5 × 1 mm compliance	46	8	0	29.08	22.96	26.70	2.46	3.42	4.16	4.84	5.69
5 × 1 mm compliance	55	12.5	0	26.88	23.20	15.90	2.41	3.75	4.24	5.00	5.71
5 × 1 mm compliance	46	8	0.1	23.08	23.46	−1.60	0.47	0.49	0.59	0.82	1.03
5 × 1 mm compliance	55	12.5	0.1	24.14	21.07	14.60	0.32	0.27	0.38	0.82	0.93

Note: [a]These values indicate that the device exhibited snap-through.

Table 3: Reverse sweep data for all devices tested.

Reverse sweep ←	Total width (mm)	Compliance length (mm)	Compression (mm)	Fr peak avg (Hz)	FEA Fn (Hz), $\zeta = 0$	% Diff.	RMS power (μW)				
							0.2	0.3	0.4	0.5	0.6
Glued pin device	46	8	0	28.38	31.29	−9.31	1.28	1.75	2.02	2.32	2.66
Glued pin device	55	12.5	0	27.96	29.68	−5.80	2.23	2.94	3.50	3.93	4.30
Glued pin device	46	8	0.1	24.52	31.17	−21.33	1.29	1.95	2.42	3.00	3.54[a]
Glued pin device	55	12.5	0.1	23.30	29.93	−22.14	3.28	4.59	5.27[a]	5.91[a]	6.60[a]
Pure pin device	46	8	0	21.22	22.82	−7.02	2.06	2.92	3.44	3.84	4.57
Pure pin device	55	12.5	0	20.52	22.41	−8.43	1.94	2.56	3.41	3.73	4.64
Pure pin device	46	8	0.1	16.32	23.41	−30.29	1.01	1.32	1.36	5.03[a]	6.16[a]
Pure pin device	55	12.5	0.1	13.82	23.20	−40.43	1.42	2.44[a]	3.56[a]	4.62[a]	5.71[a]
3 × 1, 36 mm, 0 comp	36	3	0	21.82	25.43	−14.20	3.05	3.97	4.97	5.52	6.34
3 × 1, 46 mm, 0 comp	46	8	0	23.40	20.89	12.03	3.46	4.97	5.74	6.82	7.49
3 × 1, 55 mm, 0 comp	55	12.5	0	22.02	19.85	10.96	3.21	4.67	5.03	6.06	6.68
3 × 1, 36 mm, 0.1 comp	36	3	0.1	17.16	25.27	−32.10	1.62	1.70	1.70	2.50	9.20[a]
3 × 1, 46 mm, 0.1 comp	46	8	0.1	15.24	22.57	−32.48	2.72	4.50[a]	6.73[a]	7.82[a]	9.91[a]
3 × 1, 55 mm, 0.1 comp	55	12.5	0.1	17.78	21.80	−18.43	2.01	2.00	2.00	2.09	9.89[a]
5 × 1 mm compliance	46	8	0	27.24	22.96	18.67	1.53	2.30	3.01	2.89	3.34
5 × 1 mm compliance	55	12.5	0	24.84	23.20	7.07	1.46	1.86	2.54	2.95	3.28
5 × 1 mm compliance	46	8	0.1	17.72	23.46	−24.48	1.75	2.69[a]	3.22[a]	3.54[a]	3.91[a]
5 × 1 mm compliance	55	12.5	0.1	16.40	21.07	−22.16	0.85	2.14[a]	2.84[a]	3.73[a]	4.53[a]

Note: [a]These values indicate that the device exhibited snap-through.

unbuckled states. Improvements as high as 102.2% for the forward sweeps and 53.5% for the reverse sweeps are obtained using the data in Tables 2 and 3. With the exception of the glued pinned device (which buckling always increased power in both sweep directions) buckling was a detriment until intra-well actuation was achieved. Forward sweep performance without snap-through was almost always around 80% lower than their unbuckled counterparts.

There are many different ways to characterize the performance of an energy harvester (Pellegrini et al. 2013), some of which are quite complicated due to the many different variables that can be involved (Harne and Wang 2013). Since the proposed device has a broadening effect when promoted into a high-energy state, metrics that take into account broadening effects are used. The first metric is the figure of merit (FoM) which was created by Mitcheson et al. (2008) and is expressed as

$$\mathrm{FoM}_V = \frac{16 P_{\mathrm{rms}}^{\max}}{Y_0 \rho_{\mathrm{gold}} V^{4/3} \omega^3} \quad [5]$$

where Y_0 is the input amplitude, ρ_{gold} is the density of gold, V is the volume a device occupies and ω is the peak frequency in rad/s. To account for bandwidth the FoM_V is modified by

$$\mathrm{FoM}_{\mathrm{BW}} = \mathrm{FoM}_V \frac{\mathrm{BW}_{1\,\mathrm{dB}}}{\omega_m} \quad [6]$$

where $\mathrm{BW}_{1\,\mathrm{dB}}$ is the bandwidth measured at −1 dB from the maximum power generated. The creator of the metric wanted to favor flatter frequency curves as noted by Pellegrini et al., thus measuring down from the peak power by about ~80%.

Another interesting metric to use for this device is the performance index created by Pellegrini et al. (2013) and is expressed as

$$I = \frac{P_{\mathrm{rms}} f}{m a_{\mathrm{rms}}^2} \quad [7]$$

where m is a specified mass of the oscillator. The entire mass of the device was used in evaluation and not just the proof mass due to the rest of the system making up a considerable amount of the system mass. This would yield a conservative estimate of the performance index. To get the total performance index, all performance index values are integrated over a set range as

$$I_{a-b} = \frac{\int_a^b I df}{b-a} \quad [8]$$

where a and b are frequency values picked by the user. A value of −3 dB (~50%) from the peak power generated was selected for the new bistable devices since that is where the FWHM is usually measured. I_{a-b} is typically thought of as a mean index value. The coefficient of variation for this metric which specifies a relative standard deviation is determined from

$$\mathrm{CV}_{a-b} = \frac{\sqrt{\frac{\int_a^b I^2 df}{b-a} - (I_{a-b})^2}}{I_{a-b}} \quad [9]$$

Plots showing the performance index and coefficient of variation swept in the forward direction are shown in Figure 6. The pure pinned device in the buckled configuration outperformed itself in the unbuckled configuration during HEO snap-through behavior at higher accelerations. Also, short compliance arms on the 3×1 device did give a wider spread of frequency content during HEO when compared to all other 3×1 device experiments. Reverse sweeps did not show any performance index metrics that outperformed their unbuckled case though most did approach an equivalent value to their unbuckled counterpart.

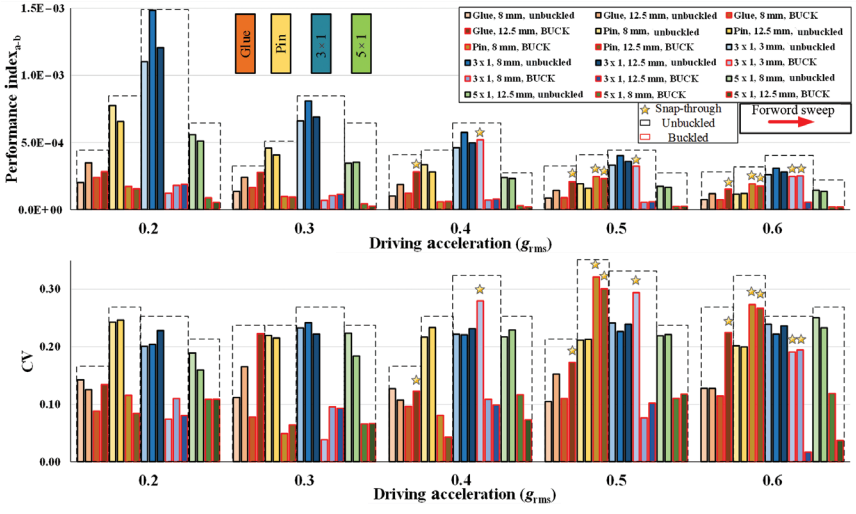

Figure 6: Performance index and coefficient of variation for all devices swept in the forward direction.

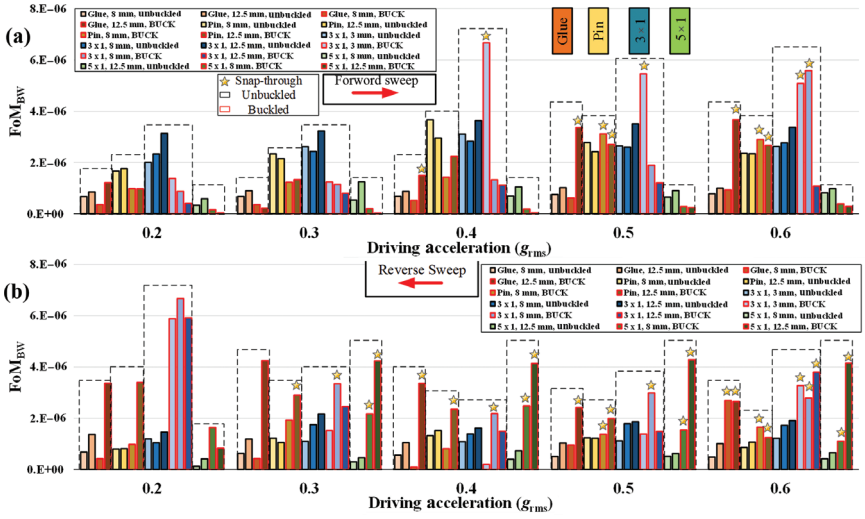

Figure 7: Figures of merit for all devices swept in the (a) forward and (b) reverse directions.

FoMs modified by a −1 dB bandwidth for all experiments in the forward and reverse cases are shown in Figure 7. From the Mitcheson metric, once a device is kicked into HEO snap-through operation, the FoM_{BW} value does outperform the unbuckled case in both the forward and reverse direction. Also the 3×1 device shows an increased metric in the reverse direction at low acceleration inputs. This is primarily due to the wide bandwidth shown in Figure 5.

Chirp Response

Determining what frequency to drive the devices at while imposing a monopulse was done by using the value found at peak performance in swept forward experiments from prior prototypes of the same geometry but swept at a faster rate. Data analysis on the power generation had not been done so it was not known whether the devices would exhibit spring stiffening or softening. To judge the stability and ease of promotion, experiments were performed at f_{p} and $\pm$ 2 Hz. Acceleration for the experiments ranged from 0.1 to 0.8 g_{rms}. Chirp tests were not performed on the glued pin version of the device. A plot of the pinned devices undergoing a chirp excitation is shown in Figure 8.

All experiments for the chirp excitation are shown in Table 4. Values in italics and blue exhibited HEO operation after an in-phase chirp and either temporarily or constantly maintained that state. During HEO operation the proof mass displacement amplitude greatly increases as well as the voltage output. Some devices would exhibit HEO for 1–3 s until ultimately going back to their normal oscillation state which could be a non-snap-through or a continuous snap-through state.

Discussion

Power generation for the devices above is not very impressive compared with other constructed VEHs when considering the size of the prototypes. This is because PVDF in a single d_{31} electrode arrangement is not very efficient at generating and collecting enough charge on a per unit strain bases. These piezoelectric elements were chosen due to their cost efficiency and design convenience (can cut any PVDF strip you like with scissors). One way to improve power output is to choose a more efficient medium like PZT or AlN.

Optimum load resistance was quite high for the PVDF strips but that was to be expected. This is the primary reason the custom data acquisition system was built, so as to not allow a parasitic load drop through the internals of the data acquisition system (DAQ) and only through the chosen load resistors. The selected optimum load resistance of 30 MΩ was within 10% of the maximum power generating performance given a constant input acceleration for all tested devices in load resistance testing.

Free damping experiments usually led to greatly different damping ratios. This is due to the sensing mechanism used, which was the PVDF electrode signal that is essentially the average strain effect of the sensing area. It is assumed that the structure buckles as if it were pinned in the middle giving no charge neutralization points over the electrodes but there still can be out-of-plane movement due to the geometry of the compliance arms. The damping

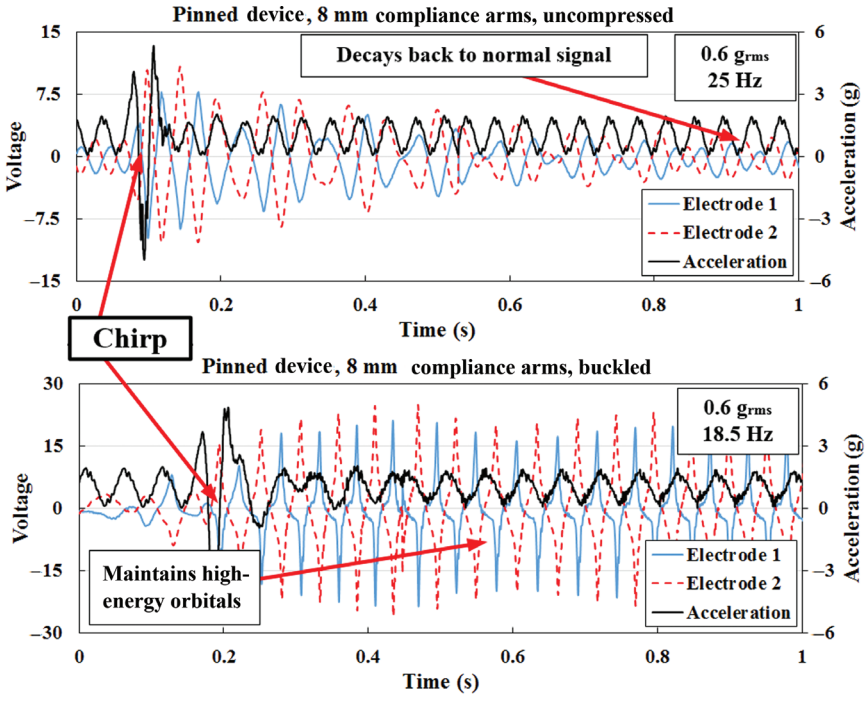

Figure 8: Chirp response of the pinned device in the unbuckled (above), compared to the maintained high-energy orbit in the buckled configuration (below).

Table 4: Chirp results for the 8 mm length compliance arm devices.

Base Accel (g_{rms})	Pinned			3 × 1 mm			5 × 1 mm		
	Fr − 2 (Hz)	Fr (Hz)	Fr + 2 (Hz)	Fr − 2 (Hz)	Fr (Hz)	Fr + 2 (Hz)	Fr − 2 (Hz)	Fr (Hz)	Fr + 2 (Hz)
0.1	18.5	20.5	22.5	22.5	24.5	26.5	22.5	24.5	26.5
0.2	17.0	19.0	21.0	22.0	24.0	26.0	21.5	23.5	25.5
0.3	*15.5*	17.5	19.5	21.5	23.5	25.5	21.0	23.0	25.0
0.4	*14.5*	*16.5*	*18.5*	21.0	23.0	25.0	20.0	22.0	24.0
0.5	14.0	*16.0*	*18.0*	20.5	22.5	24.5	19.5	21.5	23.5
0.6	*18.5*	*20.5*	22.5	*21.0*	23.0	25.0	18.5	20.5	22.5
0.7	*18.0*	*20.0*	22.0	*20.0*	22.0	24.0	*16.0*	*18.0*	*20.0*
0.8	*18.0*	*20.0*	22.0	*19.5*	21.5	23.5	*18.0*	*20.0*	22.0

Note: Italic values indicate devices that can be induced into high-energy orbits.

linear and nonlinear models give interesting results. While it is entirely appropriate to say the nonlinear model does not give an accurate damping ratio, it is worthwhile to mention that some of the buckled gain plots are not necessarily perfect representations of a spring stiffening/softening behavior. This can be seen in Figure 4(b) and also deduced from the fact that the nonlinear model should almost always give a lower damping ratio value than the linear model, given an ideal gain plot. From the outcomes, compression almost always increases the damping ratio for these VEH. It would seem that a value of 3–6% is a good estimate for the damping ratio in future FEA analysis given the data presented here.

It is interesting to note that the uncompressed devices mostly exhibited a stiffening nonlinearity due to their voltage outputs. On the other hand all of the buckled devices had a softening nonlinearity where their response was largest and broadest when swept in a reverse direction. This of course only applies to the region where snap-through is not occurring. One reoccurring aspect of snap-through and HEOs is that it seems to extend the frequency response of the device on the lower end during a reverse sweep as seen in Figure 5(d). Snap-through action of the devices almost always improves the maximum P_{rms} value obtained compared to the unbuckled case and does broaden the higher power

FWHM operating condition. The downside is that these benefits are only obtained at a sufficient input acceleration to achieve intra-well actuation. After a sufficient amount of time in the bistable regime, devices such as the 3×1 mm and pinned setup tend to kick into HEOs quite easily and can be audibly heard and seen. These performance improvements come from the fact that the device can generate higher voltages (given the same acceleration input) in HEO actuation then it can in the stochastic snap-through actuation.

The performance metric only showed the pinned device benefiting from snap-through actuation during HEO compared to the unbuckled state. This particular metric puts more emphasis on higher frequency content, which is not beneficial to our devices when measured strictly on a forward or reverse sweep basis. HEO operation shows that performance stitching is feasible, which means the actual bandwidth of the device during HEO is the overlapping power maps in the forward and reverse cases from Figure 5 (b) and (d). Combining these graphs shows that snap-through operation extends the power range significantly.

The $\mathrm{FoM_{BW}}$ metric did show that HEO operation was beneficial for all of the devices compared to their unbuckled states. It also shows that a compliance arm geometry such as the 3×1 mm device can perform just as well as a pinned device which is encouraging for a MEMS version of the energy harvester assuming the effects scale. Other works report peak power outputs of 240–280 μW, 26 Hz, 0.8 $\mathrm{m/s^2}$ (Challa et al. 2008), 300–400 μW, 200–250 Hz, 9.8 $\mathrm{m/s^2}$ (Leland and Wright 2006) and 8 mW, 67 Hz, (Cottone et al. 2014). Though the peak FoM_V (unbuckled 3×1 12.5 mm compliance, 7.33×10^{-5}), $\mathrm{FoM_{BW}}$ (buckled 3×1 3 mm compliance, 6.67×10^{-6}) or power (unbuckled 3×1 8 mm compliance, 13.3 μW) in this work is nowhere near some of the other reported VEH devices (best $\mathrm{FoM_V} = 0.68$, $P_{\mathrm{rms}} = 6$ μW) from Mitcheson et al. (2008), the device is hardly optimized at this point. More efficient piezoelectric/structural materials may be selected as well as optimized geometry modifications.

Promotion into HEOs is a fascinating aspect of bistable devices and can be induced in these prototypes at driving accelerations as low as 0.3 g_{rms}. As stated above the frequency regime chosen to do the chirp experiments was done before a full sweep data analysis, so the frequencies of the chirp analysis tended to be slightly higher than the stability region for HEO. An example of this is that the 5×1 mm device would only exhibit HEOs momentarily at 18 Hz and 0.6 g_{rms} which was the lower frequency end of the experiment but going back and repeating the 0.6 g_{rms} experiments at 16 Hz resulted in the device maintaining HEOs. Looking back at the 5×1 mm devices reverse frequency sweep chart indicated that 18 Hz was just on the cusp of the power drop-off point for that prototype.

Conclusions

The effects of compliance arms on bistable buckled devices actuated via torque are quantified. Optimum load resistance for all devices is around 30 MΩ. Peak operating frequencies are between 18 and 30 Hz and snap-through actuation occurring as low as 0.3 g_{rms}. Damping ratios are produced for free and forced scenarios below the snap-through point and had an average damping ratio of 4.1%. Nonbuckled devices generally had lower damping ratios but not by much if the devices are not overly compressed. The buckled 3×1 mm device with the shortest compliance arms generated 12.6 μW at 21.1 Hz when swept forward at 0.4 g_{rms} and was the highest $\mathrm{FoM_{BW}}$ metric of all devices tested.

Snap-through behavior increases power output (up to 102.2%) in almost all devices. Buckled glued devices outperformed all unbuckled glued devices. Devices that are buckled but do not exhibit snap-through perform significantly worse than their unbuckled counterparts (except the buckled glued device). Too much buckling increased the snap-through acceleration threshold to an unrealistic level. These bistable devices can be promoted into HEOs by applying a perturbing force. HEOs increased power output while being driven by the same input sine wave before the monopulse was applied. HEO operation tends to also broaden the operating range by enabling lower frequency content.

The glued pinned devices performed poorly in the forward sweep direction but had comparable power results in the reverse sweep. Pinned devices were the easiest to promote into HEOs. The 3×1 devices generated the most power than all other devices. The 5×1 devices performed poorly compared to the 3×1, which shows that an optimum width of the PLA compliance arms exists. Compliance arm length functioned as a snap-through performance modifier which could increase torsional resistance but prevent out-of-plane deflection, thus creating a shallower energy well hump. Compliance arm length for the glued devices did increase power as length increased because the steel rod essentially disallowed out-of-plane deflection for the lengths tested.

Acknowledgments: The authors would like to thank the University of Louisville and the Mechanical Engineering Department for their help and support during this project.

Funding: Portions of this work have been funded in part by the National Science Foundation, via award no. 1130528 through the CMMI Division and award no. 1408005 through the ECCS Division.

References

Allen, J. J. 2005. *Micro Electro Mechanical System Design*. London: CRC Press.

Amin Karami, M., and D. Inman. 2012. "Powering Pacemakers from Heartbeat Vibrations Using Linear and Nonlinear Energy Harvesters." *Applied Physics Letters* 100 (4):042901.

Ando, B., S. Baglio, A. Bulsara, and V. Marletta. 2014. "A Bistable Buckled Beam Based Approach for Vibrational Energy Harvesting." *Sensors and Actuators A: Physical* 211:153–61.

Beards, C. F. 1995. *Engineering Vibration Analysis with Application to Control Systems*. Oxford: Butterworth-Heinemann.

Challa, V., M. Prasad, Y. Shi, and T. Fisher. 2008. "A Vibration Energy Harvesting Device with Bidirectional Resonance Frequency Tenability." *Smart Material Structures* 17 (1):10.

Cottone, F., P. Basset, H. Vocca, L. Gammaitoni, and T. Bourouina. 2014. "Bistable Electromagnetic Generator Based on Buckled Beams for Vibration Energy Harvesting." *Journal of Intelligent Material Systems and Structures* 25 (12):1484–95.

Davis, W. 2011. "Measuring Quality Factor from a Nonlinear Frequency Response with Jump Discontinuities." *Journal of Microelectromechanical Systems* 20 (4):968–75.

Dementyev, A., S. Hodges, S. Taylor, and J. Smith. 2013. Power consumption analysis of bluetooth low energy, zigbee, and ant sensor nodes in a cyclic sleep scenario. In *Proceedings of IEEE International Wireless Symposium (IWS)*. IEEE.

Erturk, A., and D. Inman. 2011. "Broadband Piezoelectric Power Generation on High-Energy Orbits of the Bistable Duffing Oscillator with Electromechanical Coupling." *Journal of Sound and Vibration* 330 (10):2339–53.

Harne, R. L., and K. W. Wang. 2013. "A Review of the Recent Research on Vibration Energy Harvesting via Bistable Systems." *Smart Materials & Structures* 22 (2):023001.

Jiang, Y., S. Shiono, H. Hamada, T. Fujita, K. Higuchi, and K. Maenaka. 2010. "Low-Frequency Energy Harvesting Using a Laminated PVDF Cantilever with a Magnetic Mass." *Power MEMS* :375–8. http://cap.ee.ic.ac.uk/~pdm97/powermems/2010/

Leland, E. S., and P. K. Wright. 2006. "Resonance Tuning of Piezoelectric Vibration Energy Scavenging Generators Using Compressive Axial Preload." *Smart Materials and Structures* 15 (5):1413.

Masana, R., and M. F. Daqaq. 2011. "Relative Performance of a Vibratory Energy Harvester in Mono–and Bi-stable Potentials." *Journal of Sound and Vibration* 330 (24):6036–52.

Masana, R., and M. F. Daqaq. 2013. "Response of Duffing-Type Harvesters to Band-Limited Noise." *Journal of Sound and Vibration* 332 (25):6755–67.

Mitcheson, P. D., E. M. Yeatman, G. K. Rao, A. S. Holmes, and T. C. Green. 2008. "Energy Harvesting from Human and Machine Motion for Wireless Electronic Devices." *Proceedings of the IEEE* 96 (9):1457–86.

Pellegrini, S. P., N. Tolou, M. Schenk, and J. L. Herder. 2013. "Bistable Vibration Energy Harvesters: A Review." *Journal of Intelligent Material Systems and Structures* 24 (11):1303–12.

Percy, S., C. Knight, S. McGarry, A. Post, T. Moore, and K. Cavanagh. 2014. *Thermal Energy Harvesting for Application at MEMS Scale*. New York: Springer-Verlag.

Porter, D., and T. Berfield. 2014. "A Bi-stable Buckled Energy Harvesting Device Actuated via Torque Arms." *Smart Materials and Structures* 23 (7):075003.

Spreemann, D., B. Folkmer, and Y. Manoli. 2011. "Realization of Nonlinear Hardening Springs with Predefined Characteristic for Vibration Transducers Based on Beam Structures." MikroSystemTechnik Kongress, Darmstadt, Deutschland.

Trigona, C., F. Maiorca, B. Ando, and S. Baglio. 2013. "Tri-stable Behavior in Mechanical Oscillators to Improve the Performance of Vibration Energy Harvesters." The 17th International Conference on Solid-State Sensors, Actuators and Microsystems, Barcelona, Spain, IEEE, 458–61.

Twiefel, J., and H. Westermann. 2013. "Survey on Broadband Techniques for Vibration Energy Harvesting." *Journal of Intelligent Material Systems and Structures* 24 (11):1291–302.

Wang, N. 2010. "Fabrication and Integration of Permanent Magnet Materials into MEMS Transducers." PhD thesis, University of Florida.

Wen, L., H. MengDi, M. Bo, S. XuMing, H. XianLiang, and Z. HaiXia. 2014. "Low Frequency Wide Bandwidth MEMS Energy Harvester Based on Spiral-Shaped PVDF Cantilever." *Science in China Series E: Technological Sciences* 57 (6):1068–72.

Xu, C., Z. Liang, B. Ren, W. Di, H. Luo, D. Wang, K. Wang, and Z. Chen. 2013. "Bi-stable Energy Harvesting Based on a Simply Supported Piezoelectric Buckled Beam." *Journal of Applied Physics* 114 (11):114507.

Zheng, Y., X. Wu, M. Parmar, and D.-W. Lee. 2014. "High-Efficiency Energy Harvester Using Double-Clamped Piezoelectric Beams." *The Review of Scientific Instruments* 85 (2):026101.

Zuo, L., and X. Tang. 2013. "Large-Scale Vibration Energy Harvesting." *Journal of Intelligent Material Systems and Structures* 24 (11):1405–30.